American Mineralogist, Volume 84, pages 1535–1548, 1999

Atomically resolved electronic structure of pyrite {100} surfaces: An experimental and theoretical investigation with implications for reactivity

KEVIN M. ROSSO,[1,*] UDO BECKER,[2] AND MICHAEL F. HOCHELLA JR.[1]

[1]Department of Geological Sciences, Virginia Polytechnic Institute and State University, Blacksburg, Virginia 24061, U.S.A.
[2]Universität Münster, Institut für Mineralogie, Corrensstrasse 24, D-48149 Münster, Germany

ABSTRACT

Clean pyrite {100} surfaces, generated by cleaving in UHV, were investigated using scanning tunneling microscopy and spectroscopy for the purpose of understanding the electronic structure at the surface. Calculations of the surface atomic structure and LEED data support a {100} surface structure that undergoes very little relaxation and can be approximated by a simple termination of the bulk structure along a plane of cleaved Fe-S bonds. UPS spectra show a well defined peak at ~1 eV forming the top of the valence band for the near surface. Calculated densities of states for the bulk crystal suggest that this band is comprised primarily of non-bonding Fe 3d t_{2g} character and lesser S 3p and Fe 3d e_g character. Slab calculations predict that the loss of coordination at the surface results primarily in the displacement of Fe $3d_{z^2}$-like surface states into the bulk band gap. Evidence for this surface state is found in low bias STM imaging and normalized single-point tunneling spectra. Calculations of the LDOS at surface Fe and S sites indicate that the highest occupied state is primarily of $3d_{z^2}$-like character and the lowest unoccupied state is of mixed Fe $3d_{z^2}$-S 3p character. The results predict that due to the dangling bond surface states, Fe sites are energetically favored over S_2 sites for redox interaction with electron donors or acceptor species on this surface. Surface redox reactions are expected to involve the quenching of these high energy dangling bonds, leading to new bonds and surface species, changing the chemical makeup of the surface.

INTRODUCTION

Pyrite (FeS_2) plays an important role as an electron source in many redox-based geochemical and biogeochemical processes such as the cycling of S, Fe, and other elements in the environment (Luther et al. 1992; Calmano et al. 1994; Nimick and Moore 1994), precious metal ore deposit formation (Nash et al. 1981; Jean and Bancroft 1985; Bakken et al. 1989; Hyland and Bancroft 1989; Starling et al. 1989), and the generation of environmentally hazardous acid mine drainage (e.g., Jambor and Blowes 1994). It is also a photovoltaic semiconductor (0.9 eV bandgap) with potential applications in solar energy conversion (e.g., Bronold et al. 1994a). As such, there has been much interest in understanding the fundamental reactions involved in the oxidative dissolution of pyrite.

Most of the groundbreaking solution phase research to that end was conducted prior to the early 1980s (see references in Hiskey and Schlitt 1981; Lowson 1982; and Nordstrom 1982). Key mechanistic aspects of the oxidative process have been the topic of current spectroscopic and microscopic investigations such as the exact interaction of the oxidant with surface sites, the role of water as a reactant (i.e., Taylor et al. 1984; Reedy et al. 1991), and the influence of surface microtopography and defects to name a few. Recent contributions in this regard have highlighted the complexity of the problem at hand by identifying a variety of reactive sites, introducing the interesting possibility that distinctly different oxidation mechanisms may be proceeding across the pyrite surface (Eggleston et al. 1996; Nesbitt et al. 1998; Schaufuss et al. 1998). The issue largely hinges around the atomic structure of the pyrite surface that, when exposed by cleavage is known to be quite variable. Pyrite generally has poor cleavage quality along {100} planes and such surfaces can be macroscopically characterized as an unpredictable combination of {100} terraces and "conchoidal" deviations. Using scanning tunneling microscopy (STM) on pyrite cleaved in air, Eggleston et al. (1996) resolved true {100} surface domains at the atomic scale, which were separated by a high density of steps. There, important observations were presented of the oxidation of {100} surface iron states and the unique influence of nearest neighbor Fe on the lateral progression of oxidation. At unoxidized areas of the surface, both the highest occupied and lowest unoccupied states were attributed to Fe 3d states. Recent photoelectron spectroscopy work (Bronold et al. 1994b; Nesbitt et al. 1998; Schaufuss et al. 1998) has also identified important reactive surface sulfur states on in-vacuum cleaved pyrite, indicating the presence of monosulfide species from broken disulfide bonds formed as a result of cleavage. Similarly, reactive S-deficient defects have been observed using temperature programmed desorption (TPD) and photoemission of adsorbed xenon (PAX) on in-

*Present address: Environmental Molecular Sciences Laboratory, Pacific Northwest National Laboratory, P.O. Box 999, K8-96, Richland, Washington 99352, U.S.A. E-mail: kevin.rosso@pnl.gov

vacuum prepared (sputter/anneal cleaning cycles) pyrite {100} growth surfaces (Guevremont et al. 1997; 1998). Undoubtedly, a variety of structural sites can be present on pyrite {100}, each with their own affinities for oxidants such as O_2. But their distribution, their association with bulk and cleavage induced defects, and their role in the overall oxidation of pyrite remain as important unresolved issues.

Collectively, previous work has underscored the importance of understanding the atomic and electronic structure of surface sites via a local probe such as STM. In this paper, we investigate pristine pyrite surfaces, cleaved in ultra-high vacuum (UHV), using scanning tunneling microscopy and spectroscopy (STM-STS), ultraviolet photoelectron spectroscopy (UPS), low energy electron diffraction (LEED), and theoretical calculations with a goal of understanding the site specific electronic structure of the {100} surface. Large flat {100} terraces and these are the primary focus of this contribution. To our present knowledge, we present the first atomically resolved tunneling spectra on any geochemically significant natural material. This investigation is meant to elucidate the site-specific variables of primary importance to the initial stages of oxidation of the {100} surface, and to aid in future investigations of pyrite surface chemistry.

METHODS

Principal instrumentation

All the experimental techniques were performed in an OMICRON compact UHV laboratory operating at a base pressure of 1×10^{-10} mbar. The main chamber is equipped with a dual anode (Al,Mg) X-ray source, UV lamp, ion gun, a reverse view LEED with a 1 keV electron gun, cylindrical sector electron energy analyzer, and a sample heater capable of attaining 750 °C. The system is also equipped with an in-house built gas leak manifold for controlled gas bleeds to various parts of the main chamber. A side chamber contains the STM stage, its vibration isolation and eddy current damping system, and the in-vacuum tunneling electronics.

Samples

Natural pyrite single crystal cubes from Logroño, Spain (the Museum of Geological Sciences at Virginia Tech) were cut into approximately $5 \times 5 \times 10$ mm oriented prisms with faces cut perpendicular to the principal crystallographic axes. The resistivity of one of the samples was measured to be 3×10^{-4} Ω·m using a four-point probe and Hall voltage measurements on the same sample indicated that it is an n-type semiconductor. Pridmore and Shuey (1976) attribute n-type behavior to trace substitutions of Co, Ni, or Cu for Fe, and found consistent semiconducting characteristics for pyrites from similar geologic environments. Hence, we assumed that all our samples were n-type. Samples with visible inclusions were discarded. The samples were mechanically mounted in custom stainless steel stubs and cleaved using an in-house built cleavage stage in the load-lock chamber which is turbo-pumped to better than 1×10^{-7} mbar. The prisms were slightly notched around the mid-section to control fracture propagation. Samples cleaved in the load-lock chamber, were quickly transferred to the lower base pressure of the main chamber in less than 30 seconds.

Low energy electron diffraction

LEED patterns were acquired using 4-grid reverse view LEED optics (OMICRON) at beam energies between 70–300 eV. The electron gun has a beam diameter of approximately 1 mm. Diffraction patterns were photographically recorded. The data were collected immediately after turning up the beam energy because the intensity and sharpness of the diffraction spots were found to degrade within a few minutes. The surface cell dimension was determined using the measured separation between diffraction spots arising from the reciprocal face-centered cubic lattice.

Ultraviolet photoelectron spectroscopy

UPS spectra were collected using He I (21.2 eV) radiation, a pass energy of 10 eV, and a collection angle of approximately 0 degrees. The sample stubs, the outsides and the notches in the pyrite prisms used in the UPS experiments were sputter coated with a visible layer of Au to isolate the Fe spectral data to that coming from the cleaved surface. Ten spectral scans were collected over a period of 10 minutes to average out noise. The absolute binding energy scale of the UPS spectra was referenced to the sample Fermi level, which was determined by subtracting 21.2 eV from the low kinetic energy photoelectron cutoff energy and adding the workfunction of the spectrometer. The low kinetic energy edge was designated at the energy half way between the 16 and 84% count rate levels at the cutoff. The measurement of the workfunction of the spectrometer is based on the measured position of the Ag $3d_{5/2}$ photo peak.

Scanning tunneling microscopy and spectroscopy

The STM tip is rastered using a tripod piezo scanner with a 1.2 μm maximum lateral scan range. The bias voltage is applied to the sample while the tip is held at ground potential. Tips for imaging and spectroscopy were prepared by electrochemically etching W wire in 1 *M* KOH. As indicated in the caption, one measurement used pre-cut commercial Pt-Ir tips (Digital Instruments). Surfaces with large, flat terraces were targeted for atomic-scale imaging. It turned out that the most ideal tunneling conditions for atomically resolved images were at low negative bias voltages, between –0.40 to –0.02 V, using a 1 nA setpoint current. For larger scale topographic imaging, 1 V and 1 nA were used to increase the tip-sample distance and avoid tip crashes. Larger scale images were processed by fitting and subtracting a planar background. Atomically resolved images that required processing to remove noise were band pass fast fourier transformed (FFT) filtered by passing the frequencies pertaining to "topographic" features (low frequency) and atomic periodicity. Samples and tips were stored under base pressure in a carousel attached to the main chamber. Samples were shielded from light during all STM imaging, and images were collected at room temperature.

Tunneling spectra [current as a function of voltage, (I(V)] were collected using a variation of current imaging tunneling spectroscopy (CITS) mode over 1 nm^2 imaging areas on a well-developed {100} terrace. At each spectroscopy point, the tip raster was paused, the feedback loop was turned off, the voltage ramp was applied, the loop was re-engaged, and imaging resumed. Spectra were collected at room temperature, which

has been estimated to have a maximum energy resolution of ~100 mV taking into account thermal broadening effects (Hansma 1982; Chen 1993). All spectra were collected in the dark unless otherwise noted. Because the most successful imaging conditions were at very low bias for atomically resolved images, the tip-sample distance was relatively small. During the voltage ramp at a spectral point, the exponentially increasing tunneling current would quickly saturate the current-to-voltage converter (50 nA maximus). Because of an instrumental control limitation, the tip-sample separation could not be adjusted simultaneously during the voltage ramp, a technique known as the varying-gap method (Mårtensson and Feenstra 1989; Feenstra 1994). To collect wide dynamic range spectra, tunneling conditions were re-optimized for a larger tip-sample separation for spectral data collection. Using 4 V and 7 nA allowed a –4 to +4 V dynamic range in the voltage ramp. The raw $I(V)$ curves were converted to $(dI/dV)/(I/V)$ using a least-squares moving window fit. This form can remove the tip-sample separation dependence of the tunneling conductance under certain conditions (Feenstra et al. 1987) and can provide information that is related to the density of states of the sample under the assumption that the tip density of states is constant. The mathematical spike at low bias was suppressed by adding a small constant to I/V across the entire voltage range before the conversion.

Ab initio calculations

Ab initio calculations were performed using Gaussian94 (Frisch et al. 1995) for gas phase cluster calculations, and Crystal95 for periodic systems (Dovesi et al. 1996). The computer platforms utilized were two DEC Alpha stations and an IBM SP2 at Virginia Tech. For the Gaussian94 calculations, after investigating various cluster sizes and basis sets and weighing in the factor of computational expense, a 27-atom stoichiometric cluster was chosen to model the pyrite {100} surface. It is a charge neutral section of the bulk face-centered cubic crystal structure: nine atomic layers by nine atomic layers by six atomic layers thick. The basis set used was a standard 6-311G. Polarization functions were not added to the basis set. The wavefunctions were calculated using a Hartree-Fock density functional theory hybrid method using the Becke3LYP functional (Becke 1993). For the Crystal95 calculations, an electron core pseudopotential (ECP) basis set was used. Specifically, a LANL2DZ set (Hay and Wadt 1985a, 1985b) was used in which the net core charges attributed to the Fe (1s,2s,2p) and the S (1s,2s,2p) orbitals are mimicked by pseudopotential functions. This is justified because these orbitals are not expected to contribute state density near the Fermi level. The basis set was modified by removing diffuse functions with gaussian exponents <0.1, which are usually not appropriate for the crystalline case (see Pisani 1996), and the exponent of the most diffuse function on Fe was optimized. The sensitivity of the calculated DOS and projected DOS to changes in this exponent was tested and it was found to have a negligible effects. The Kohn-Sham wavefunctions were calculated at the unrestricted DFT level of theory using the Lee-Yang-Parr (Lee et al. 1988) correlation potential and the Becke (Becke 1988) exchange potential. The 45 k-points (Monkhorst net) were sampled in the irreducible part of the Brillouin zone (shrinking factors 8 8 16, see Pisani 1996). Fock matrix mixing and Fermi-level shifting techniques were implemented to overcome slow SCF convergence.

Local densities of states (LDOS) were calculated for comparison with experimental normalized tunneling spectra using the methods similar to those described in Becker and Hochella (1996), which are based on the assumptions of Tersoff and Hamman (1985). The comparison can only be made under the assumption that the effects of the tip electronic structure are negligible. The LDOS of the sample at locations of the tip was computed by summation of the contributions of the atomic orbitals to the molecular orbitals that fall within a specified energy range (the bias voltage). Because the basis sets are gaussian functions which tail-off relatively quickly, they poorly describe the true decay of wavefunctions normal to the surface. This means that the calculated LDOS at the location of the tip at normal tunneling distances of 3–10 Å from the surface is nil. Although there are more sophisticated ways to attack this problem (see Becker and Hochella 1996), a reduced tip-sample distance of 1 Å was used to obtain an approximation of the LDOS of surface sites. Also, because the cluster is treated from a molecular orbital theory approach and not a periodic approach, the state densities were convoluted with gaussian functions (FWHM = 0.5 eV), with unity areas and centered at eigenvalues, to mimic the dispersion of states into bands and account for the resolution of the experimental spectra.

RESULTS AND DISCUSSION

Surface microtopography and atomic structure

Bulk pyrite is face-centered cubic with a structure that is reminiscent of the rocksalt structure type. A characteristic aspect of the pyrite structure is the S_2 anion pair which is oriented along body diagonals of the cubic cell (Fig. 1). Prediction of the surface structure largely revolves around the question of whether or not the covalent S-S bond preferentially remains intact during cleavage. The lowest energy (i.e., lowest dipole moment) {100} surface is formed from the cleavage of Fe-S bonds only, assuming for the moment that no significant reconstruction occurs. However, because pyrite is known to have poor cleavage along {100}, it is reasonable to assume that S-S bonds are also broken when the fracture deviates from {100}. A recent reinterpretation of the S 2p and Fe 2p photoemission spectra on cleaved pyrite supports this assumption and attributes the resulting monosulfide species to areas of non-{100} congruency (Nesbitt et al. 1998). Because it seems very likely that the proportion of such structural domains on the surface will be dependent on the specific sample and method of cleaving, it was important for the purposes of this study to engage the problem of characterizing the surface atomic structure.

LEED is an area-averaged probe that provides information on long range atomic periodicity of atoms within the first few monolayers of a surface. Non-periodic defects are not resolved. LEED patterns of the freshly cleaved surface were bright and sharp with no pronounced background, but tended to degrade to weaker patterns in a matter of a few tens of seconds due to electron beam damage. The patterns were dominated by intense diffraction spots characteristic of the reciprocal face centered cubic cell (Fig. 2). Less intense spots with half the

periodicity are derived from the c (2×2) superstructure of the disulfide groups (Pettenkofer et al. 1991). The LEED patterns are consistent with exposure of the {100} surface but do not provide insight into the larger scale surface microtopography. Calculation of the surface cell constant from the LEED patterns yields a value of 5.45 Å which compares reasonably well with the accepted bulk lattice constant of 5.42 Å, indicating that lateral structural relaxation along {100} is insignificant and supporting the observations of Pettenkofer et al. (1991). However, structural relaxation to some degree perpendicular to the plane of the surface is typical to compensate for lost bonding symmetry at surface sites (Jaegermann and Tributsch 1988; Hochella 1990; Zangwill 1988). The magnitude of vertical relaxation does not appear to be significant in case of the pyrite {100} surface. Ab initio cluster calculations on the 27-atom pyrite cluster were performed with no symmetry constraints to investigate the magnitude of structural relaxation. The lowest energy configuration involved minimal structural displacement with a maximum atomic coordinate displacement of less than 0.1 Å for non-edge site atoms. Collectively, the LEED and cluster results suggest that the {100} surface atomic structure can be regarded as simple termination of the bulk. However, this does not mean that the electronic structure is unchanged at the surface.

Topographic, or Z-piezo voltage (Z), UHV STM images at scales of several hundred nanometers demonstrated that the microtopography of the cleavage surfaces in this study was dominated by flat, stepped terraces. Representative images (Fig. 3) show the flat surfaces that were generated by cleavage, typically terminated by unit cell high steps. The images and LEED results suggest that pyrite cleaves surprisingly well along the cubic axes at this scale, exposing {100} surfaces. Furthermore, crystallographic control is demonstrated in preferred step edge directions along the two dimensions of the surface, oriented along <10> and/or <21> as in Figures 3a–c. Areas within step density were relatively high (Fig. 3d), although the step edge direction is still along a principal crystallographic axis. Such areas are very similar to those reported in Eggleston et al. (1996) and may be related to domains typically characterized as "conchoidal." Step edge control was, for the most part, pronounced, but not exclusive as shown in Figure 3e where curved steps were found, indicating a high kink density along these step edges. Areas on the large, flat terraces of the surface were targeted for the high resolution STM-STS data collection in this study.

Bulk and surface electronic structure

The electronic structure of bulk pyrite has been studied at length from the perspective of either molecular orbital theory

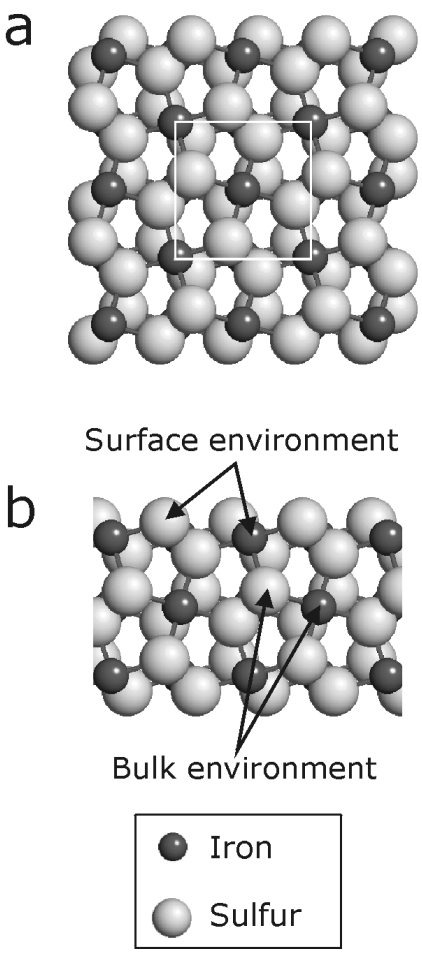

FIGURE 1. Ball and stick model of the pyrite {100} surface showing the 9-monolayer periodic slab used to calculate the projected densities of states for bulk and surface environments in pyrite. Dark spheres = Fe atoms; Light spheres = S atoms.

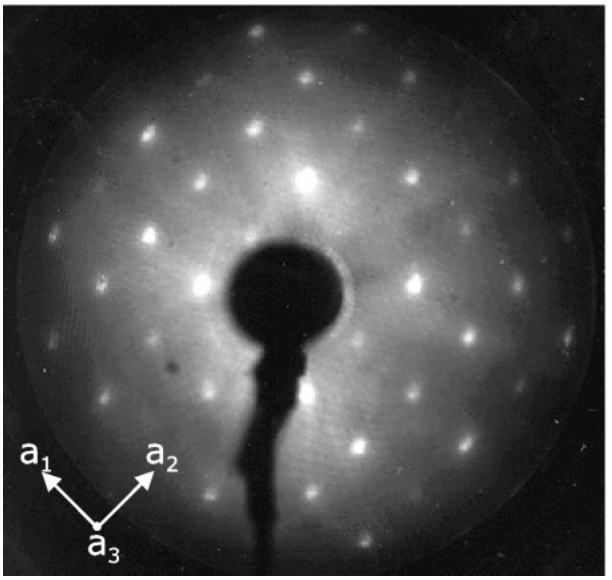

FIGURE 2. LEED image of in-vacuum cleaved pyrite {100}. The image was collected using a beam energy of 134.6 eV. The crystal was oriented as indicated by the axes.

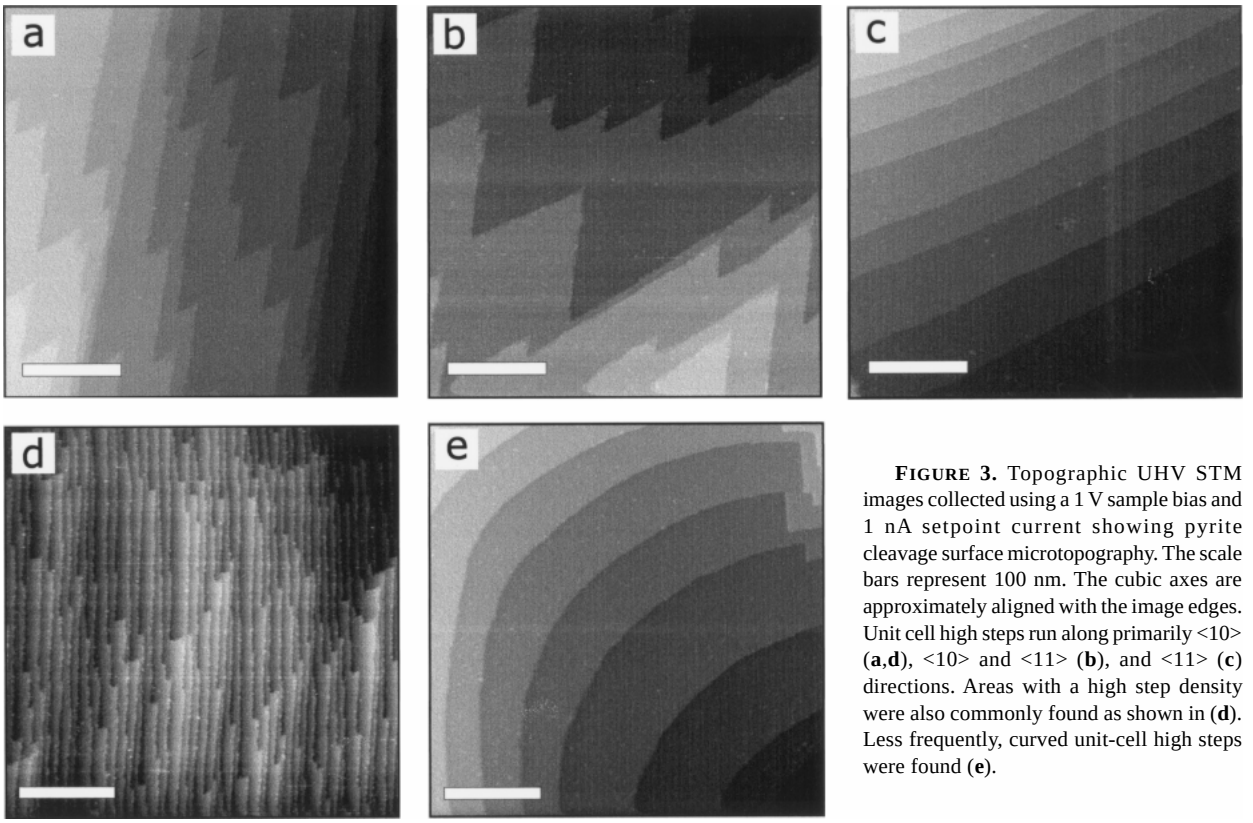

FIGURE 3. Topographic UHV STM images collected using a 1 V sample bias and 1 nA setpoint current showing pyrite cleavage surface microtopography. The scale bars represent 100 nm. The cubic axes are approximately aligned with the image edges. Unit cell high steps run along primarily <10> (**a**,**d**), <10> and <11> (**b**), and <11> (**c**) directions. Areas with a high step density were also commonly found as shown in (**d**). Less frequently, curved unit-cell high steps were found (**e**).

or band theory (Bither et al. 1968; Burns and Vaughan 1970; Li et al. 1974; Ogawa et al. 1974; Schlegel and Wachter 1976; Van der Heide et al. 1980; Bullett 1982; Folmer et al. 1988; Ferrer et al. 1990; Huang et al. 1993; Mosselmans et al. 1995; Bocquet et al. 1996; Charnock et al. 1996; Raybaud et al. 1997; Eyert et al. 1998) and will only be summarized here as a starting point for the discussion of the surface electronic structure. The upper part of the valence band consists of predominantly a non-bonding Fe 3d t_{2g} band which lies above a bonding S 3p-Fe 3d e_g band. As measured using UPS, there is a characteristic peak in the density of states at the top of the valence band at approximately 1.1 eV which has been overwhelmingly attributed primarily to the non-bonding t_{2g}-like states (Fig. 4a). The lower part of the conduction band is well regarded to be dominated by Fe 3d e_g^*-like states, although there are recent arguments for the substantial presence of S 3p states (Eyert et al. 1998). Fe 4s states do not contribute significantly in the upper part of the valence band studied here. The accepted bulk band gap is ~0.9 eV as measured using a variety of experimental techniques.

Using Crystal95, we calculated the valence band density of states (DOS) for the bulk crystal (periodic in 3 dimensions) and the {100} surface (periodic slab in 2 dimensions) and projected the results onto atomic orbitals which could contribute state density to the top of the valence band, which are the Fe 3d and S 3p states. In the bulk case (Fig. 4b), the top of the valence band is predominantly of non-bonding Fe 3d t_{2g} character, as has been previously determined (see references above), but consists of appreciable Fe 3d e_g and S 3p character as well (Fig. 4b). These states lie above a bonding Fe 3d-S 3p band (3–7 eV) and S 3p band (7–10 eV). States below this latter band are not included in the calculation as they are modeled by core pseudopotentials. The results indicate that the e_g states form a relatively broad band (~6 eV wide) while the t_{2g} states are largely non-bonding and restricted to a narrow energy range (FWHM ~1 eV) at the top of the valence band. Like the e_g states, the S 3p states are widely dispersed between 1–8 eV.

At the surface, the degeneracies within the t_{2g} and e_g states are lost as a consequence of the lower bonding symmetry. The effect of the reduction in the Fe coordination from the distorted octahedron to roughly square pyramidal on the d orbital states has been addressed qualitatively using ligand-field theory (LFT) (Jaegermann and Tributsch 1988; Birkholz et al. 1991; Bronold et al. 1994b). To avoid confusion, we note that the e_g orbitals referred to in the electrostatic framework of ligand field theory are analogs to the antibonding counterpart (e_g*) of the low-lying e_g set involved in the Fe-S sigma bond in the framework of band theory (see references at the start of this section).

A nine monolayer thick slab was chosen to model the {100} surface electronic structure (Fig. 1b). Upper valence band state density localized on Fe atoms at the surface were compared with that from Fe atoms located in the middle of the slab (Fig. 5), which are fully coordinated and can be taken to represent the bulk sites. According to the slab calculations, the removal

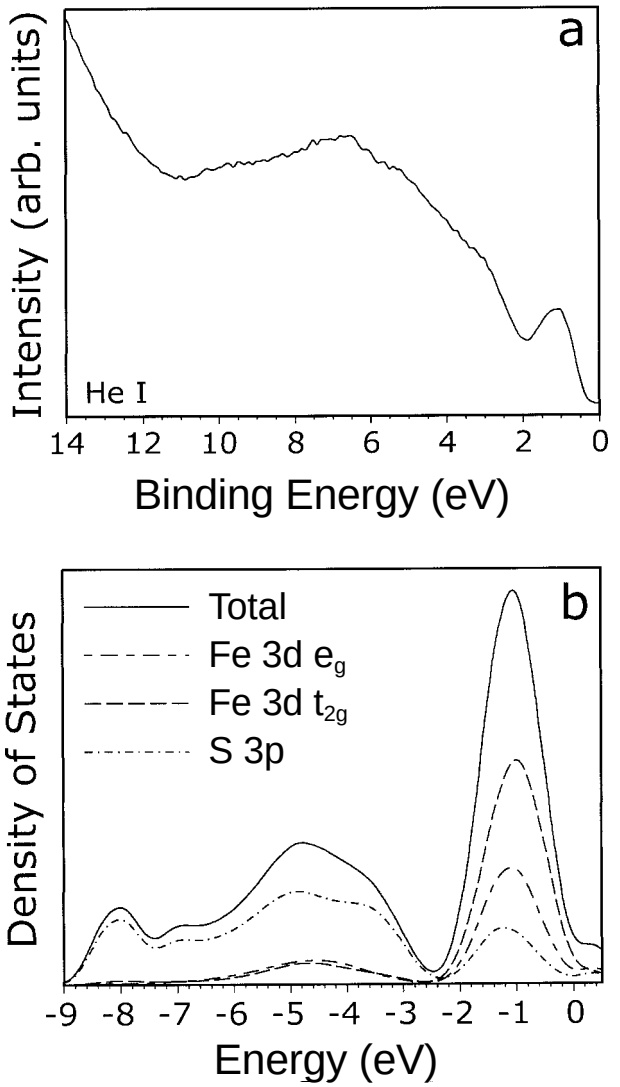

FIGURE 4. (**a**) He I UPS valence band spectra of an in-vacuum cleaved pyrite {100} surface. (**b**) Calculated total and projected densities of states for the valence band of bulk pyrite. The contributions primarily arise from Fe 3d and S 3p states.

of an Fe-S bond and the loss of overlap with S 3p orbitals energetically destabilizes every Fe d orbital with a z-component (z arbitrarily chosen normal to the surface plane). This effect is primarily seen in the shift of Fe d_{z^2} states to higher energy, but also in the slight destabilization of d_{xz} and d_{yz} states relative to d_{xy}. The former result is compatible with predictions of LFT, but the latter is not in that LFT predicts that d_{xy} should be located at higher energy than d_{xz} and d_{yz} (Bronold et al. 1994b). Regarding the conflict, our results are inconclusive but may be an indication of minor bonding overlap between the Fe t_{2g} set and orbitals of sulfur before cleavage, as first suggested by Burns and Vaughan (1970) and recently re-affirmed by Eyert et al. (1998). In any case, the destabilization of d_{z^2} states is more substantial and has greater significance for interpreting the STM-STS data in this study. Finally, in contrast to the Fe 3d states, our calculations indicate that surface S 3p states are not energetically shifted relative to bulk S 3p states (Fig. 5).

Based on LFT, Bronold et al. (1994b) proposed that the low spin property of bulk pyrite (d^6) could be converted to high-spin at the {100} surface. This could have implications for the sorption of paramagnetic species such as O_2 (see Becker and Hochella 1996) as well as impact the interpretation of Fe 2p XPS spectra (Nesbitt et al. 1998). However, our calculations, performed using open shell techniques (see methods section), suggest no such unpairing of Fe 3d electrons exists at the {100} surface. Attempts were made to locate low total energy unpaired spin solutions for the slab. The calculations were started using a spin-unbalanced constraint for several initial self-consistent cycles, but the spin configuration always reverted to low spin when the restriction was lifted. Extracting a spin pairing energy from our calculations for comparison with that of Bronold et al. (1994b) is not practical so further work is required to reconcile these separate observations.

The most significant difference between the bulk and surface electronic structures is then, at the surface, Fe d_{z^2} states are displaced above the essentially non-bonding d_{xy}, d_{xz}, and d_{yz} states. This result suggests that the energy of these d_{z^2} states should be within the bulk band gap, meeting the formal definition of surface states. The calculations make no such indication for S 3p states on this surface and so here, it is assumed that they contribute negligible surface state density. Normally, the presence of surface states leads to atomic reconstruction, reducing the surface free energy (see Zangwill 1988). But based on surface structural evidence to the contrary in this case, these surface states should be preserved in vacuum and are thus best described as dangling bonds.

Atomic scale scanning tunneling microscopy

Surfaces of pyrite have been previously studied at high resolution using STM in air (Eggleston and Hochella 1990; Fan and Bard 1991; Eggleston and Hochella 1992; Siebert and Stocker 1992; Eggleston 1994; Eggleston et al. 1996). Interpretation of the image data in chemical terms is seldom straightforward, but when coupled with theoretical calculations, it can be done profitably. Because electrons occupying the highest energy filled states are the least tightly bound, they have the longest decay lengths away from the surface into the vacuum. For STM, the implications are that the states which are closest to the Fermi level of the negatively biased electrode (either the sample or the tip) are the primary contributors to the tunneling current. In the case of a negatively biased sample, electrons tunnel primarily from a narrow energy range of the highest filled states of the sample into empty states of the tip. For a pristine pyrite {100} surface in vacuum, this means that Fe sites should be high tunneling current sites at negative bias because the highest energy filled states are Fe 3d dangling bonds. Furthermore, should the dangling bond states be only partially occupied, Fe sites should appear as high tunneling current sites at low positive bias voltage as well.

Atomic scale UHV STM observations are consistent with these assertions. Topographic (*Z*) and current (*I*) image data show an array of high tunneling current sites, the symmetry

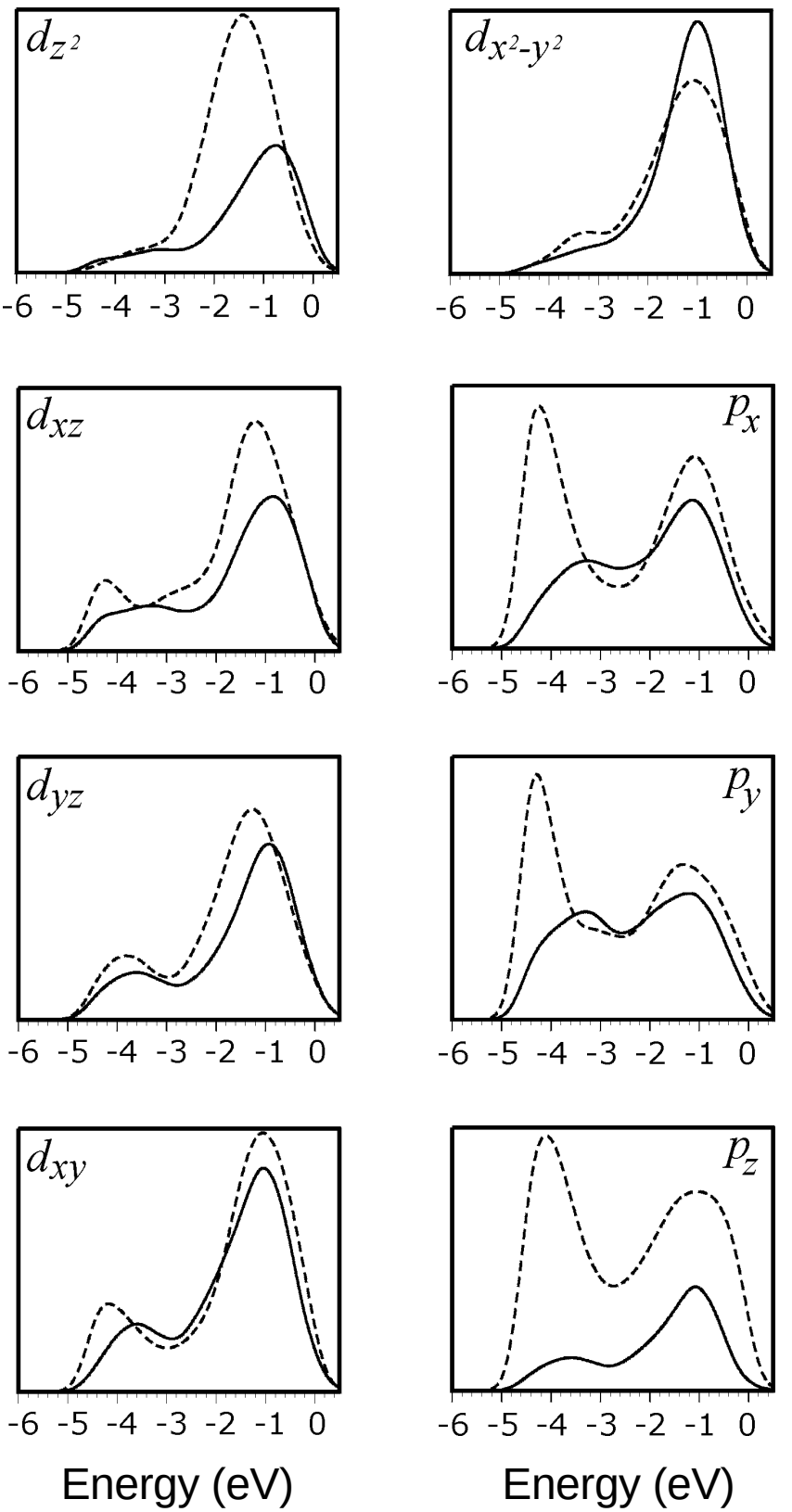

FIGURE 5. Calculated projected densities of states for the Fe 3d and S 3p states in both bulk (dotted lines) and surface (solid lines) environments in pyrite.

and spacing of which are consistent with the face centered cubic array of Fe atoms within a {100} plane of the structure (Fig. 6). As shown best in Figure 6a, a step edge and corner is imaged in the lower right corner. The step height, as measured using a topographic profile, is ~2.5 Å corresponding to roughly half of a unit cell edge. An atomically resolved, half unit cell high step edge is in Figure 6e and 6f. The step edge direction along the surface for half unit cell high steps is usually preferential to <11> directions although <10> control has also been observed.

Images identical to those described above were obtained most successfully at a variety of low bias voltages within the bulk band gap (–400 to –20 mV and +20 to +140 mV) (Fig. 7a). Attempts to collect images at biases lower than ±20 mV resulted in tip scouring of the pyrite surface. Sets of images collected at positive and negative biases simultaneously (dual-mode STM) were obtained down to within ±20 mV of the Fermi level (Figs. 7b and 7c). These images show 1 to 1 correspondence of the location of high tunneling current sites, indicating that both the highest occupied and the lowest unoccupied states are localized at surface Fe sites. The narrow voltage range used to collect these images is probably an indication that there is either a surface gap that is no greater than 40 meV, or that the density of surface states is continuous but somewhat reduced closer to the Fermi level. In either case, when combined with the slab calculation results, it can be logically argued that the high tunneling current sites in the dual-mode STM images correspond to partially filled Fe d_{z^2}-like dangling bond surface states.

A model of the electronic structure of the pyrite surface is shown diagrammatically in Figure 8 for n-type pyrite. Equilibration between the pyrite bulk and Fe dangling bond states, located in the bulk band gap, involves filling the surface states up to the position of the bulk Fermi level (Fig. 8a). The charge occupying the surface states constitutes a potential which repels bulk electrons from approaching the surface, resulting in an upward bending of the bulk bands at the surface (Fig. 8a). Equilibration between the tip and sample Fermi levels (Fig. 8b), and the application of bias voltage to the tunneling contact (Figs. 8c and 8d) involves essentially no change in surface electronic structure of the sample. Under conditions of applied bias, electrons originate from (small negative bias, Fig. 8c) or tunnel to (small positive bias, Fig. 8d) surface states at Fe sites. From a molecular orbital theory perspective, these form the highest occupied (HOMO) and lowest unoccupied molecular orbitals (LUMO). The fact that both the HOMO and LUMO states at the surface are localized on Fe sites is an indication that both electron donor and acceptor species sorbed to the surface should interact primarily with Fe sites.

Scanning tunneling spectroscopy

Area-averaged spectra. Area-averaged tunneling spectra (Fig. 9a) were collected to elucidate the overall energetic distribution of state density at the surface on both sides of the Fermi level. The valence band DOS acquired using tunneling spectroscopy (Fig. 9b) is in good agreement with that acquired using UPS (Fig. 4a), especially when one considers the remarkable differences in the data acquisition mechanisms. Both spectra show a prominent feature at the top of the valence band, a peak that we have already been able to ascribe to mostly Fe 3d and minor S 3p states. It can be reasoned, however, that the relative contribution of atomic orbitals to the density of states as measured by the two methods should be somewhat different. The kinetic energy range of the photopeak at the top of the valence band equates to an electron attenuation length of ~20 Å (Seah and Dench 1979) which means that, although UPS is surface sensitive, there is an appreciable contribution of bulk states to the spectrum, i.e., the Fe 3d t_{2g} states. In contrast, tunneling spectroscopy is sensitive only to sample states at the location of the tip, which in this case should be the dangling bond states and S 3p states. The presence of surface state density within the bulk band gap has also been observed using tunneling spectroscopy on pyrite in air (Fan and Bard 1991; Eggleston et al. 1996).

Revealing the energetic location of the band edges using tunneling spectroscopy is a problematic task. As can be seen in the area-averaged spectrum (Fig. 9a), the apparent width of the surface gap is much larger than the dual-mode STM images indicate. The reason for this is partly due to a low signal-to-noise ratio for large tip-sample distances, and partly due to a loss of spectral information arising from the well-known mathematical divergence of the $(dI/dV)/(I/V)$ calculation at very low current values. For semiconductor surfaces, during the collection of $I(V)$ spectra, the tunneling current approaches zero faster than the bias voltage as the voltage ramp approaches the Fermi level from either direction. Very low current values at finite bias voltages cause the denominator to go to zero and the normalized curve to have a spike in the gap. This artifact can be suppressed by adding a small constant to the denominator over the whole curve, at the expense of spectral information in the band gap region. At the same time, the "steepness" of the $I(V)$ curve and the width of this flat, low current region is dependent on the tip sample distance. Large tip-sample separations give large low current regions around the Fermi level and thus poorer signal-to-noise ratios for spectral information from the gap region. However, large separations are needed for wide dynamic range in the $I(V)$ curve using a fixed tip-sample separation during data collection. Smaller tip-sample separations are needed for spectral data near the Fermi level, at the expense of wide dynamic range. For these reasons, the area-averaged spectrum in this study lacks spectral details near the Fermi level and gives an underestimation of the density of states within the bulk band gap.

Single-point spectra. Single-point spectra were also collected in an attempt to take advantage of the potential of tunneling spectroscopy to resolve LDOS features at specific surface sites. For pyrite, unfortunately the optimal tunneling conditions for collecting atomically resolved images and that for wide dynamic range tunneling spectra are very different. Because of this, and because we could not implement the varying-gap method (see "Methods"), we collected tunneling spectra independent of atomically resolved images.

Collection of meaningful single-point spectra on freshly cleaved pyrite in UHV proved to be very difficult and only in the rarest cases were we able to attain stable tunneling contact during $I(V)$ collection giving a high signal-to-noise ratio. Suc-

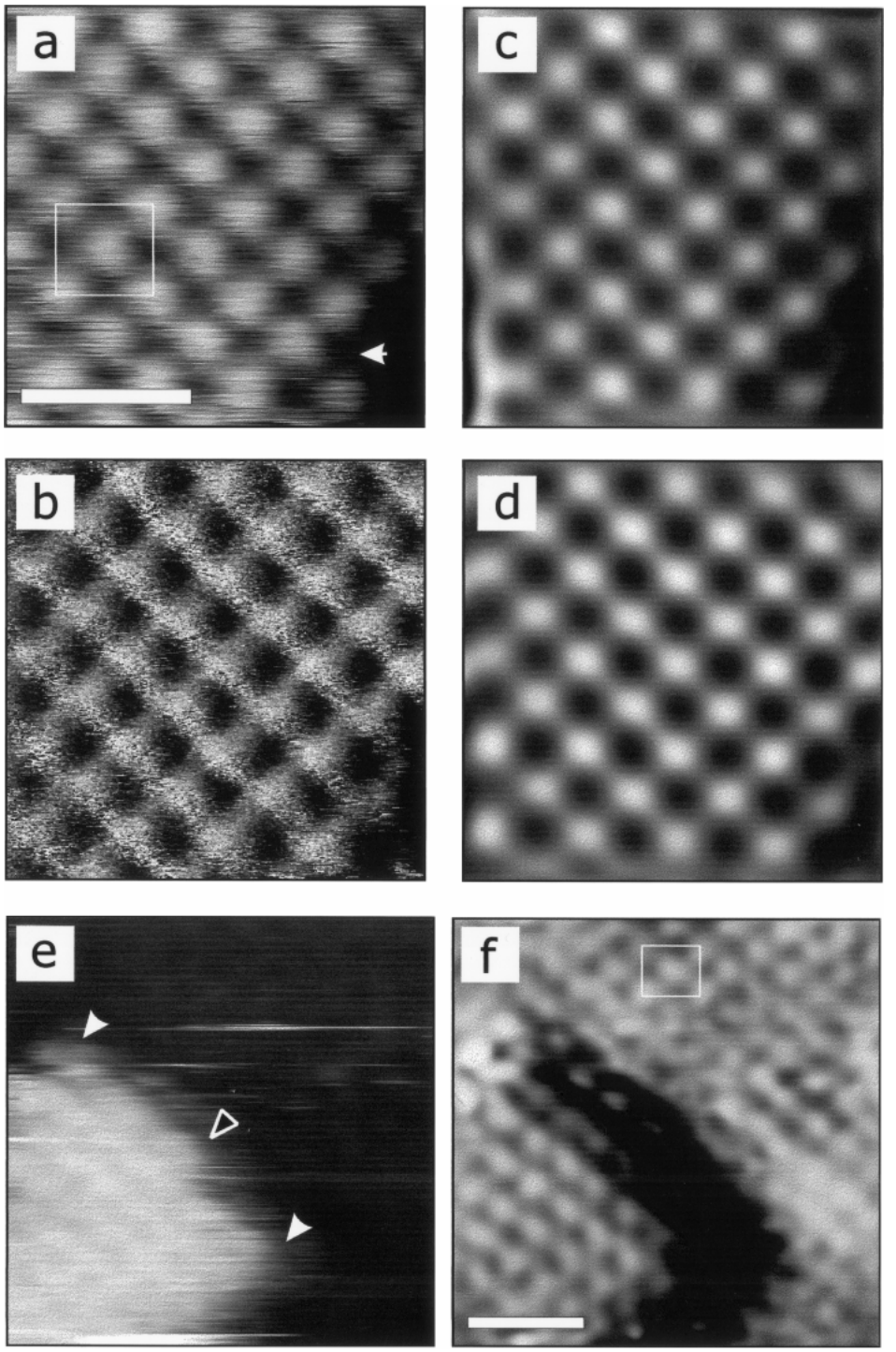

FIGURE 6. Atomic-scale raw topographic (**a**) and current (**b**) UHV STM images of in-vacuum cleaved pyrite {100}. Image edges are roughly aligned with crystallographic axes of the simgle crystal sample. The z direction is perpendicular to the page. The images in (**c**) and (**d**) are low-pass FFT filtered images of (**a**) and (**b**), respectively. The scale bar represents 10 Å in all the images. The lower-right corner of (a) shows a half-unit cell high step edge. The solid white arrow in (a) points to a corner site in the step edge. The tunneling conditions for **a**–**d** were –0.2 V bias and 2 nA setpoint current. Two terraces separated by a half-unit cell high step are shown in topographic (**e**) and current (**f**) images collected in a different area from (**a–d**). Solid and outlined white arrows in (**e**) point to corner and kink sites along the step edge, respectively. The face-centered cubic surface cell (with some unavoidable image distortion) is outlined in (**f**). The step edge runs along <11> surface directions. The tunneling conditions were –0.1 V bias and 1.4 nA setpoint current. Images (**e**) and (**f**) are FFT filtered as described in the experimental section.

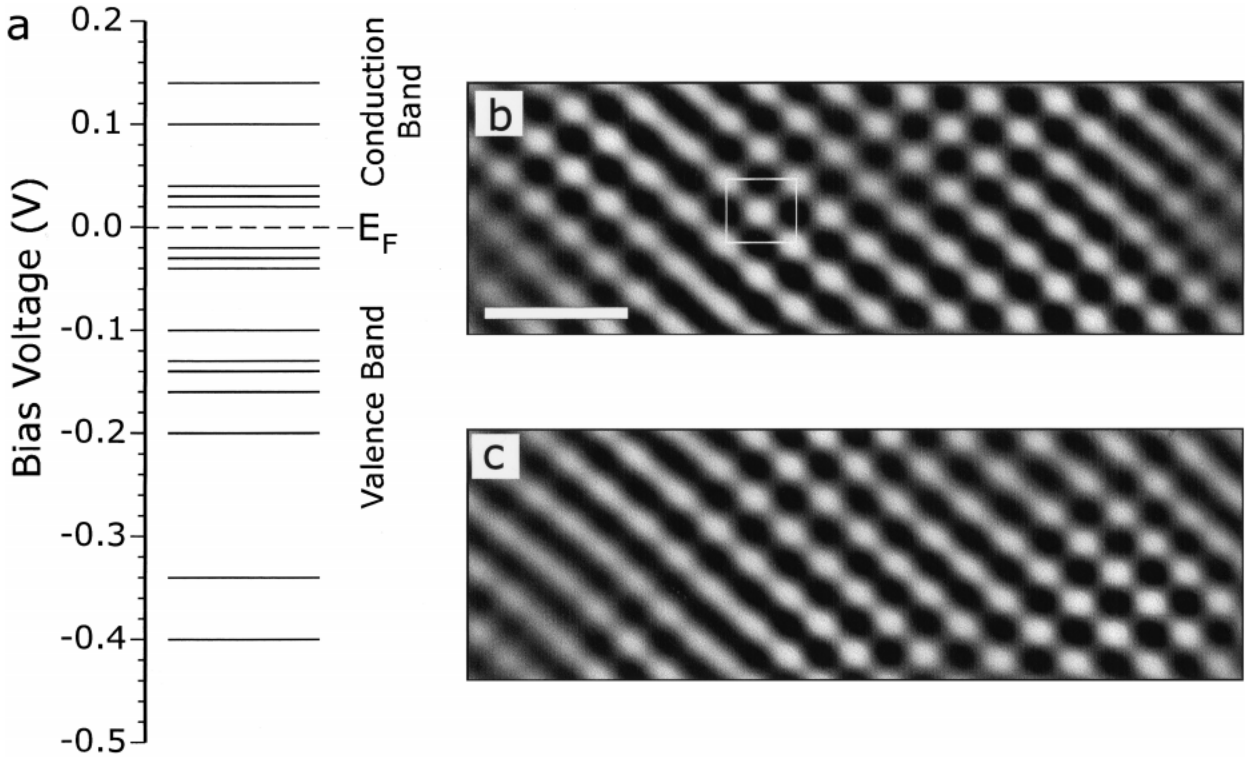

FIGURE 7. (**a**) Diagram showing the bias voltage values corresponding to atomically resolved UHV STM images. All of the images showed a face-centered cubic array of bright and dark spots consistent with the expected distribution of surface Fe sites. Dual-mode UHV STM images collected simultaneously at –0.14 V bias and 1.4 nA setpoint current (**b**), and 0.14 V bias and 1.0 nA setpoint current (**c**). The scale bar represents 10 Å. A face-centered cell is outlined in (**b**). The locations of the high and low tunneling current sites show approximate 1 to 1 correspondence between the images.

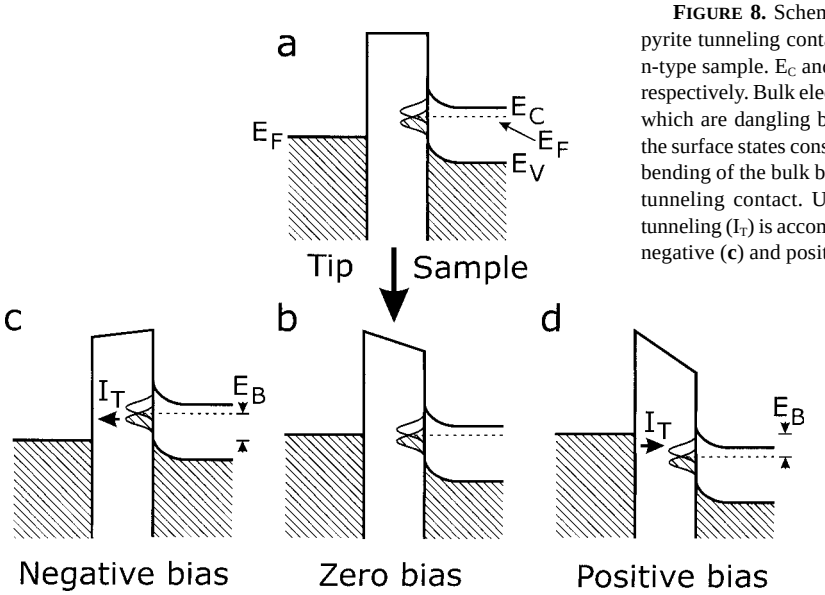

FIGURE 8. Schematic band structure diagrams modeling the tip-pyrite tunneling contact. (**a**) Thermal disequilibrium between tip and n-type sample. E_C and E_V are the conduction and valence band edges, respectively. Bulk electrons at the Fermi energy infill the surface states, which are dangling bonds localized at Fe sites. Electrons occupying the surface states constitute a surface potential which causes an upward bending of the bulk bands at the surface. (**b**) The zero-bias tip-sample tunneling contact. Under conditions of applied bias (E_B), electron tunneling (I_T) is accommodated primarily by surface states at both small negative (**c**) and positive (**d**) sample bias.

cessful spectra collected were generally one of two types. The representative spectra (Fig. 9b) show that the maximum intensity at the top of the valence is at approximately –0.8 or –2.0 eV, and the maximum intensity at the bottom of the conduction band is at 1.2 or 1.6 eV. The density of states near the Fermi level and the locations of the band edges are better represented by the single point spectra compared to the area-averaged spectrum, but they are still subject to the same difficulties as discussed above. Based on the STM imaging results and the insight provided by the ab initio calculations indicating the presence of surface states localized on Fe, we assert that the spectra showing a prominent peak at –0.8 eV (smaller surface gap) are probably collected over surface Fe sites (high tunneling current sites) and the spectra showing a prominent peak at –2 eV (larger surface gap) must be collected over S_2 sites (low tunneling current sites).

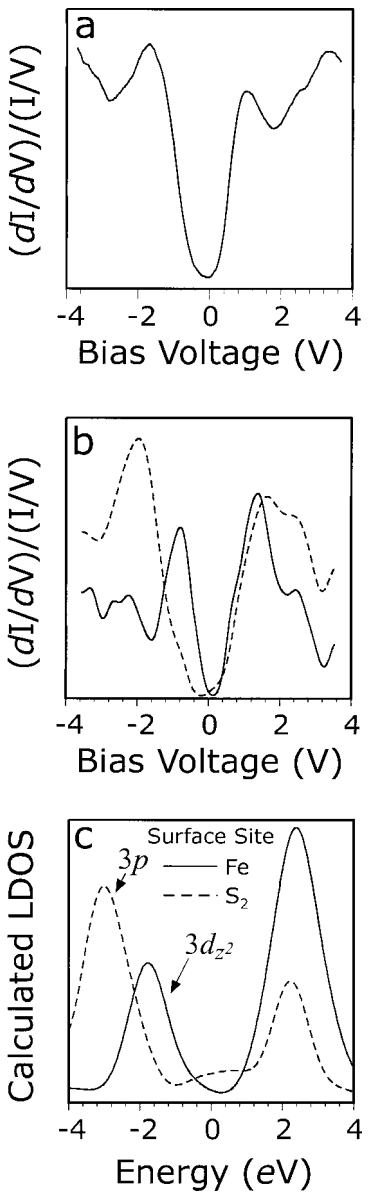

FIGURE 9. (**a**) Area-averaged normalized (d*I*/d*V*)/(*I*/*V*) tunneling spectrum collected over a random distribution of points on in-vacuum cleaved pyrite. The spectrum is the average of 90 spectra collected from several different freshly cleaved crystals with two separate W tips. (**b**) Single-point normalized tunneling spectra collected on a pristine pyrite surface. (**c**) Calculated local densities of states for tip positions over surface sites. Contributions to the LDOS over surface Fe and S_2 sites originate primarily from Fe $3d_{z^2}$-like dangling bond states and S 3p states, respectively.

The site-specific state density distributions elucidated by the single-point spectra are consistent with the STM observations in several ways. The filled component of the dangling bond states is the primary source of state density, and therefore tunneling current, on the order of bond lengths away from the surface, at negative bias voltage. Because electrons populating these states have the longest decay lengths and, at negative bias, the transmission probability is highest for states closest to the Fermi level of the sample (Hamers 1993), they should dominate the tunneling current at any negative bias voltage. Indeed, all the successful atomically resolved STM images collected in this study showed a face centered cubic arrangement of high tunneling current sites at negative bias consistent with Fe sites. "Contrast reversal" is not expected in the STM images at negative bias even though the LDOS over S sites becomes greater than that for Fe deeper in the valence band (Fig. 9b). However, at positive bias, the source of long decay length electrons is derived from the narrow portion of the top of the tip valence band [0 to ~0.3 eV (Hamers 1993)] that probe unoccupied electronic states of the sample. This leads to somewhat higher resolution at positive sample bias than for negative (Hamers 1993). Based on the single-point spectra, contrast reversal is expected at high positive bias (approximately > +2 V), where S sites should become brighter than Fe sites. So far, attempts to confirm this assertion have been unsuccessful.

The STM images conclusively show that the lowest energy unoccupied states are localized on Fe sites. This is a imaging result that is not readily revealed in the tunneling spectra due to the poor behavior of the (d*I*/d*V*)/(*I*/*V*) conversion near the Fermi level as previously discussed. The observation that the difference in the density of unoccupied states between Fe and S sites is small higher into the conduction band may explain the difficulties in achieving atomic resolution images higher at positive bias (up to ~1.2 V). Atomic imaging requires significant tunneling current contrast between sites (Chen 1993), as would not be the case for positive bias voltages in the vicinity of +1 V.

Calculated local densities of states

For comparison with the experimental spectra, we calculated the LDOS for points positioned over Fe and S_2 dimer sites using Gaussian94, and also calculated projected LDOS using atomic orbitals which could contribute to state density near the Fermi level (Fe 3d, S 3p) (Fig. 9c). Calculations of the type often overestimate the band gap due to difficulties in the estimation of the energy attributed to correlation interaction between electrons. Although the peak positions in the calculated LDOS are shifted, there are remarkable similarities with the experimental spectra. Both show a narrower gap over Fe sites, a 1.2 eV difference between the maxima for the top of the va-

lence band over Fe vs. S sites, and that the bottom of the conduction band is at similar energies for both surface sites. Again it is interesting to note that this last observation provides an explanation for the fact that STM imaging at atomic resolution on pyrite is more difficult in UHV at positive bias voltage as opposed to negative.

The LDOS projected onto Fe 3d and S 3p orbitals show that, at surface Fe sites, the highest energy filled state is predominantly due to a $3d_{z^2}$-like dangling bond. The conduction band minimum at the surface is due to both Fe $3d_{z^2}$ and S 3p states. For the S states, which are not energetically displaced at the surface, this is consistent with theoretical calculations (Eyert et al. 1998) showing that the bulk conduction band minimum consists of significant contributions from S 3p orbitals. The S site LDOS is composed of entirely S 3p states on both sides of the Fermi level within the energy range shown. Non-bonding Fe 3d states do not contribute significantly to the LDOS over surface Fe sites, but make small contributions for tip positions slightly displaced along surface Fe-Fe directions. This behavior is consistent with the fact that the non-bonding orbitals are oriented along body diagonals of the unit cell and do not project perpendicular to the plane of the surface. Hence, the smaller peaks which are observed in the experimental spectrum for surface Fe sites at ~–2.4 eV (Fig. 9b) may be derived from non-bonding Fe 3d states, given the reasonable assumption that the spectrum was collected somewhat off-center over an Fe site.

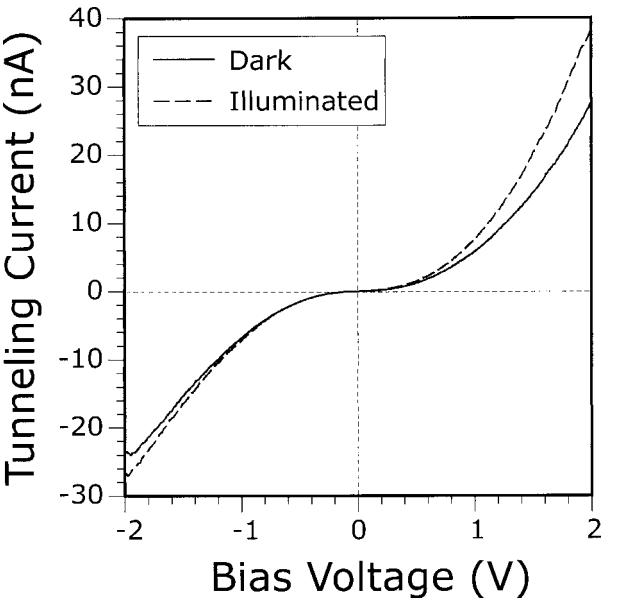

FIGURE 10. Area-averaged *I*(*V*) tunneling spectra collected on in-vacuum cleaved pyrite comparing the tunneling current response in the dark vs. illuminated conditions. Each spectrum is the average of 25 curves collected with a Pt-Ir tip.

Beam-induced surface alteration

We observed that incandescent light from a fiber optic W-filament lamp used to illuminate the STM chamber could modify the *I*(*V*) behavior of the tunneling contact (Fig. 10). Illuminated, freshly cleaved samples tended to show more Ohmic behavior with a more rapid rise in tunneling current as a function of bias voltage, especially for the positive bias ramp.

Pyrite is well known to be photoactive, the effects of which can significantly alter the chemical behavior of its surfaces (Ennaoui et al. 1986; Jaegermann and Tributsch 1988; Schubert and Tributsch 1990; Mishra and Osseo-Asare 1992; Bronold et al. 1994a). Previous work in this area has addressed the physical aspects of this photo-induced effect. However, a related phenomenon was encountered that has not been previously discussed. It was found that the surface conductivity of in-vacuum cleaved pyrite {100} is altered by exposing the surface to UV light, as would be used for UPS measurements. The behavior was assessed during attempts to engage and image surfaces that had been previously analyzed using He I UPS. Establishing tunneling contact with such surfaces, usually using a bias voltage of +1 V and a setpoint current of 1 nA, repeatedly resulted in tip crashes, on samples that had been successfully imaged before they were irradiated with UV light. Similar behavior was observed for samples that had been exposed to Al$K\alpha$ X-rays for XPS, and low-energy electron beams for LEED, except to a lesser degree. The tip would engage these surfaces, but the tunneling contact was invariably unstable which precluded the collection of high quality images. This effect is perhaps related to the experimental observation that the quality of LEED images would degrade in a matter of minutes after exposing the surface to the electron beam, which is not an uncommon phenomenon (Brundle 1974). LEED images of the UV irradiated surface were qualitatively indistinguishable from the non-irradiated surface, so we suggest that the effect is purely electronic, with possible ties to changes in the energy and occupation of surface states due to photo-induced production of electron-hole pairs and charge trapping at the surface (Jaegermann and Tributsch 1988; Osseo-Asare 1993). We did not attempt to quantify this behavior for the purposes of this study, nor is it known whether or not this effect is reversible. At this point, we only suggest that such behavior is noteworthy and that it has obvious implications for future UHV surface studies of pyrite.

Surface damage and alteration by UV and other types of incident radiation was an unexpected discovery that should be a vital consideration in future pyrite surface studies. The fact that the surface electronic structure is dominated by dangling bonds means that at least the initial interactions between sorbing species and the surface will be driven by the quenching of high energy surface states at Fe sites. This process is expected to lead to new bonds between an adsorbate and surface iron sites, implying that the chemical "makeup" of the surface that is later presented to reactants in air or solution is fundamentally different. This issue is explored further in a companion paper that follows on the interaction of these surfaces with H_2O-O_2 mixtures (Rosso et al. 1999).

ACKNOWLEDGMENTS

The manuscript benefited greatly from reviews by D.R. Strongin and H.W. Nesbitt. We thank David Cox, John Dillard, Jerry Gibbs, and Don Rimstidt for helpful comments as well. Samples were generously supplied by Susan Eriksson at the Museum of Geological Sciences at Virginia Tech. Jean Plymale, Bill Sydor, and the rest of the support staff at the computing center at Virginia Tech gener-

ously helped with hardware/software questions. We appreciate the assistance provided by Jerome Long and Dan Smith for the Hall Effect measurements and machining, respectively. The support of the National Science Foundation through grants EAR-9527092 and EAR-9628023 is gratefully acknowledged.

REFERENCES CITED

Bakken, B.M., Hochella, M.F. Jr., Marshall, A.F., and Turner, A.M. (1989) High resolution microscopy of gold in unoxidized ore from the Carlin mine, Nevada. Economic Geology, 84, 171–179.

Becke, A.D. (1988) Density-functional exchange-energy approximation with correct asymptotic behavior. Physical Review A, 38, 3098–3100.

——(1993) Density-functional thermochemistry. III. The role of exact exchange. Journal of Chemical Physics, 98, 5648–5652.

Becker, U. and Hochella, M.F. Jr. (1996) The calculation of STM images, STS spectra, and XPS peak shifts for galena: New tools for understanding mineral surface chemistry. Geochimica et Cosmochimica Acta, 60, 2413–2426.

Birkholz, M., Fiechter, S., Hartmann, A., and Tributsch, H. (1991) Sulfur deficiency in iron pyrite (FeS_{2-x}) and its consequences for band-structure models. Physical Review B, 43, 11926–11936.

Bither, T.A., Bouchard, R.J., Cloud, W.H., Donohue, P.C., and Siemons, W.J. (1968) Transition metal pyrite dichalcogenides. High-pressure synthesis and correlation of properties. Inorganic Chemistry, 7, 2208–2220.

Bocquet, A.E., Mamiya, K., Mizokawa, T., Fujimori, A., Miyadai, T., Takahashi, H., Môri. M., and Suga, S. (1996) Electronic structure of 3d transition metal pyrites MS_2 (M=Fe, Co, or Ni) by analysis of the M 2p core-level photoemission spectra. Journal of Physics, Condensed Matter, 8, 2389–2400.

Bronold, M., Pettenkofer, C., and Jaegermann, W. (1994a) Surface photovoltage measurements on pyrite (100) cleavage planes: Evidence for electronic bulk defects. Journal of Applied Physics, 76, 5800–5808.

Bronold, M., Tomm, Y., and Jaegermann, W. (1994b) Surface states on cubic d-band semiconductor pyrite (FeS_2). Surface Science Letters, 314, L931–L936.

Brundle, C.R. (1974) The application of electron spectroscopy to surface studies. Journal of Vacuum Science and Technology, 11, 212–224.

Bullett, D.W. (1982) Electronic structure of 3d pyrite- and marcasite-type sulphides. Journal of Physics C, 15, 6163–6174.

Burns, R.G. and Vaughan, D.J. (1970) The interpretation of the reflectivity behavior of ore minerals. American Mineralogist, 55, 1576–1586.

Calmano, W., Förstner, U., and Hong, H. (1994) Mobilization and scavenging of heavy metals following resuspension of anoxic sediments from the Elbe river. In American Chemical Society Symposium Series, 550, 298–321.

Charnock, J.M., Henderson, C.M.B., Mosselmans, J.F.W., and Pattrick, R.A.D. (1996) 3d transition metal L-edge X-ray absorption studies of the dichalcogenides of Fe, Co, and Ni. Physics and Chemistry of Minerals, 23, 403–408.

Chen, C.J. (1993) Introduction to scanning tunneling microscopy, 412 p. Oxford Science Publications, Oxford.

Dovesi, R., Saunders, V.R., Roetti, C., Causà, M., Harrison, N.M., Orlando, R., and Aprà, E. (1996) CRYSTAL95 user's manual, 170 p. University of Torino, Torino.

Eggleston, C.M. (1994) High resolution scanning probe microscopy: Tip-surface interaction, artifacts, and applications in mineralogy and geochemistry. In Clay Minerals Society Workshop Lectures, 7, 1–90.

Eggleston, C.M. and Hochella, M.F. Jr. (1990) Scanning tunneling microscopy of sulfide surfaces. Geochimica et Cosmochimica Acta, 54, 1511–1517.

——(1992) Scanning tunneling microscopy of pyrite {100}: Surface structure and step reconstruction. American Mineralogist, 77, 221–224.

Eggleston, C.M., Ehrhardt, J.-J., and Stumm, W. (1996) Surface structural controls on pyrite oxidation kinetics: An XPS-UPS, STM, and modeling study. American Mineralogist, 81, 1036–1056.

Ennaoui, A., Fiechter, S., Jaegermann, W., and Tributsch, H. (1986) Photoelectrochemistry of highly quantum efficient single-crystalline n-FeS_2 (pyrite). Journal of the Electrochemical Society, 133, 97–106.

Eyert, V., Höck, K.-H., Fiechter, S., and Tributsch, H. (1998) Electronic structure of FeS_2: The crucial role of electron-lattice interaction. Physical Review B, 57, 6350–6359.

Fan, F.-R. and Bard, A.J. (1991) Scanning tunneling microscopy and tunneling spectroscopy of n-type iron pyrite (n-FeS_2) single crystals. Journal of Physical Chemistry, 95, 1969–1976.

Feenstra, R.M. (1994) Tunneling spectroscopy of the (110) surface of direct-gap III-V semiconductors. Physical Review B, 50, 4561–4570.

Feenstra, R.M., Stroscio, J., and Fein, A., (1987) Tunneling spectroscopy of the Si (111) 2×1 surface. Surface Science, 181, 295–306.

Ferrer, I.J., Nevskaia, D.M., de las Heras, C., and Sánchez, C. (1990) About the band gap nature of FeS_2 as determined from optical and photo-electrochemical measurements. Solid State Communications, 74, 913–916.

Folmer, J.C.W., Jellinek, F., and Calis, G.H.M. (1988) The electronic structure of pyrites, particularly CuS_2 and $Fe_{1-x}CuSe_2$: An XPS and Mossbauer study. Journal of Solid State Chemistry, 72, 137–144.

Frisch, M.J. et al. (1995) Gaussian 94 (Revision C.2) Gaussian, Inc., Pittsburgh, Pennsylvania.

Guevremont, J.M., Strongin, D.R., and Schoonen, M.A.A. (1997) Effects of surface imperfections on the binding of CH_3OH and H_2O on FeS_2 (100): Using adsorbed Xe as a probe of mineral surface structure. Surface Science, 391, 109–124.

Guevremont, J.M., Strongin, D.R., and Schoonen, M.A.A. (1998) Photoemission of adsorbed Xenon, X-ray photoelectron spectroscopy, and temperature-programmed desorption studies of H_2O on FeS_2 (100). Langmuir, 14, 1361–1366.

Hamers, R.J. (1993) Methods of tunneling spectroscopy with the STM. In D.A. Bonnell, Ed., Scanning tunneling microscopy and spectroscopy: Theory, techniques, and applications, p. 51–103. VCH, New York.

Hansma, P. (1982) Tunneling spectroscopy: Capabilities, applications, and new techniques, 493 p., Plenum, New York.

Hay, P.J. and Wadt, W.R. (1985a) Ab initio effective core potentials for molecular calculations. Potentials for the transition metal atoms Sc to Hg. Journal of Chemical Physics, 82, 270–283.

——(1985b) Ab initio effective core potentials for molecular calculations. Potentials for main group elements Na to Bi. Journal of Chemical Physics, 82, 284–310.

Hiskey, J.B. and Schlitt, W.J. (1981) Aqueous oxidation of pyrite. In Proceedings of the 2nd SME-SPE International Solution Mining Symposium, Denver CO, 55–74.

Hochella, M.F. Jr., (1990) Atomic structure, microtopography, composition, and reactivity of mineral surfaces. In Mineral-water interface geochemistry, Reviews in Mineralogy, 23, 87–132.

Huang, Y.S., Huang, J.K., and Tsay, M.Y. (1993) An electrolyte electroreflectance study of FeS_2. Journal of Physics: Condensed Matter, 5, 7827–7836.

Hyland, M.M. and Bancroft, G.M. (1989) An XPS study of gold deposition at low temperatures on sulphide minerals: Reducing agents. Geochimica et Cosmochimica Acta, 53, 367–372.

Jaegermann, W. and Tributsch, H. (1988) Interfacial properties of semiconducting transition metal chalcogenides. Progress in Surface Science, 19, 1–167.

Jambor, J.L. and Blowes, D.W. (1994) Short course handbook on environmental geochemistry of sulfide mine-wates, 438 p. Mineralogical Association of Canada.

Jean, G.E. and Bancroft, G.M. (1985) An XPS and SEM study of gold deposition at low temperature on sulphide minerals. Geochimica et Cosmochimica Acta, 49, 979–987.

Lee, C., Yang, W., and Parr, R.G. (1988) Development of the Colle-Salvetti correlation-energy formula into a functional of the electron density. Physical Review B, 37, 785–789.

Li, E.K., Johnson, K.H., Eastman, D.E., and Freeouf, J.L. (1974) Localized and bandlike valence electron states in FeS_2 and NiS_2. Physical Review Letters, 32, 470–472.

Lowson, R.T. (1982) Aqueous oxidation of pyrite by molecular oxygen. Chemical Reviews, 82, 461–497.

Luther, G.W., Kostka, J.E., Church, T.M., Sulzberger, B., and Stumm, W. (1992) Seasonal iron cycling in the salt-marsh sedimentary environment: The importance of ligand complexes with Fe(II) and Fe(III) in the dissolution of Fe(III) minerals and pyrite, respectively. Marine Chemistry, 40, 81–103.

Mårtensson, P. and Feenstra, R.M. (1989) Geometric and electronic structure of antimony on the GaAs (110) surface studied by scanning tunneling microscopy. Physical Review B, 7744–7753.

Mishra, K.K. and Osseo-Asare, K. (1992) Fermi-level pinning at pyrite (FeS_2)/electrolyte junctions. Journal of the Electrochemical Society, 139, 749–752.

Mosselmans, J.F.W., Pattrick, R.A.D., van der Laan, G., Charnock, J.M., Vaughan, D.J., Henderson, C.M.B., and Garner, C.D. (1995) X-ray absorption near-edge spectra of transition metal disulfides FeS_2 (pyrite and marcasite), CoS_2, NiS_2, and CuS_2, and their isomorphs FeAsS and CoAsS. Physics and Chemistry of Minerals, 22, 311–317.

Nash, J.T., Granger, H.C., and Adams, S.S. (1981) Geology and concepts of important types of uranium deposit. Economic Geology, 75th Anniversary Volume, 63–116.

Nesbitt, H.W., Bancroft, G.M., Pratt, A.R., and Scaini, M.J. (1998) Sulfur and iron surface states on fractured pyrite surfaces. American Mineralogist, 83, 1067–1076.

Nimick, D.A. and Moore, J.N. (1994) Stratigraphy and chemistry of sulfidic floodplain sediments in the Upper Clark Fork Valley, Montana. In American Chemical Society Symposium Series, 550, 276–288.

Nordstrom, K.D. (1982) Aqueous pyrite oxidation and the consequent formation of secondary minerals. In J.A. Kittrick, D.S. Fanning, and L.R. Hossner, Eds., Acid Sulfate Weathering: Pedogeochemistry and Relationship to Manipulation of Soil Materials: Madison, Wisconsin, p. 37–56. Soil Science Society of America Press, Madison, Wisconsin.

Ogawa, S., Waki, S., and Teranishi, T. (1974) Magnetic and electrical properties of 3d transition-metal disulfides having the pyrite structure. International Journal of Magnetism, 5, 349–360.

Osseo-Asare, K. (1993) Pyrite in aqueous systems: Semiconductor properties, oxidative dissolution, and environmental control. In H. Henein and T. Oki, Eds., First International Conference on Processing Materials for Properties. The Minerals, Metals & Materials Society, Warrendale, Pennsylvania.

Pettenkofer, C., Jaegermann, W., and Bronold, M. (1991) Site specific surface interaction of electron donors and acceptors on FeS_2 (100) cleavage planes. Berichte der Bunsen-Gesellschaft fur Physikalische Chemie, 95, 560–565.

Pisani, C. (1996) Quantum-mechanical ab-initio calculation of the properties of crystalline materials, 327 p., Springer-Verlag, Berlin.

Pridmore, D.F. and Shuey, R.T. (1976) The electrical resistivity of galena, pyrite,

and chalcopyrite. American Mineralogist, 61, 248–259.
Raybaud, P., Hafner, J., Kresse, G., and Toulhoat, H. (1997) Ab initio density functional studies of transition-metal sulphides: II. Electronic structure. Journal of Physics: Condensed Matter, 9, 11107–11140.
Reedy, B.J., Beattie, J.K., and Lowson, R.T. (1991) A vibrational spectroscopic ^{18}O tracer study of pyrite oxidation. Geochimica et Cosmochimica Acta, 55, 1609–1614.
Rosso, K.M., Becker, U., and Hochella, M.F. Jr. (1999) The interaction of pyrite {100} surfaces with O_2 and H_2O: Fundamental oxidation mechanisms. American Mineralogist, 84, 1549–1561.
Schaufuss, A.G., Nesbitt, H.W., Kartio, I., Laajalehto, K., Bancroft, G.M., Szargan, R. (1998) Reactivity of surface chemical states on fractured pyrite. Surface Science, 411, 321–328.
Schlegel, A. and Wachter, P. (1976) Optical properties, phonons and electronic structure of iron pyrite (FeS_2). Journal of Physics C, 9, 3363–3369.
Schubert, B. and Tribatsch H. (1990) Photoinduced electron transfer by coordination chemical pathways across pyrite/electrolyte interfaces. Inorganic Chemistry, 29, 5041–5046.
Seah, M.P. and Dench, W.A. (1979) Quantitative electron spectroscopy of surfaces: A standard data base for electron mean free paths in solids. Surface and Interfacial Analysis, 1, 2–11.
Siebert, D. and Stocker, W. (1992) Investigation of a (100) surface of pyrite by STM. Physica Status Solidi A, 134, K17–K20.
Starling, A., Gilligan, J.M., Carter, A.H.C., Foster, R.P., and Saunders, R.A. (1989) High-temperature hydrothermal precipitation of precious metals on the surface of pyrite. Nature, 340, 298–300.
Taylor, B.E., Wheeler, M.C., and Norstrom, D.K. (1984) Stable isotope geochemistry of acid mine drainage: Exerimental oxidation of pyrite. Geochimica et Cosmochimica Acta 48, 2669–2678.
Tersoff, J. and Hamann, D.R. (1985) Theory of the scanning tunneling microscope. Physical Review B, 31, 805–813.
Van der Heide, H., Hemmel, R., van Bruggen, C.F., and Haas, C. (1980) X-ray photoelectron spectra of 3d transition metal pyrites. Journal of Solid State Chemistry, 33, 17–25.
Zangwill, A. (1988) Physics at surfaces, 454 p. Cambridge University Press, Cambridge.

MANUSCRIPT RECEIVED JULY 16, 1998
MANUSCRIPT ACCEPTED JUNE 4, 1999
PAPER HANDLED BY GLENN A. WAYCHUNAS